minerals

MDPI

Article

Geochronology and Geochemistry of Ore-Hosting Rhyolitic Tuff in the Kengdenongshe Polymetallic Deposit in the Eastern Segment of the East Kunlun Orogen

Ya-Yun Liang [1,*], Rui Xia [2,*], Xiaoyu Shan [1], Yao Ma [3], En-Quan Zhao [3,4] and Wenhui Guo [1]

1 School of Civil and Resource Engineering, University of Science and Technology Beijing, Beijing 100083, China; xy.shan@xs.ustb.edu.cn (X.S.); s20180002@xs.ustb.edu.cn (W.G.)
2 Comprehensive Survey Command Center for Natural Resources, China Geological Survey, Beijing 100055, China
3 State Key Laboratory of Geological Processes and Mineral Resources, China University of Geosciences (Beijing), Beijing 100083, China; 3001180004@cugb.edu.cn (Y.M.); 2001170014@cugb.edu.cn (E.-Q.Z.)
4 Langfang Natural Resources Integrated Survey Center, China Geological Survey, Langfang 065000, China
* Correspondence: liangyayun@ustb.edu.cn (Y.-Y.L.); xiaruiren@126.com (R.X.); Tel.: +86-010-62333930 (Y.-Y.L.); +86-010-82340922 (R.X.)

Received: 8 July 2019; Accepted: 25 September 2019; Published: 28 September 2019

Abstract: The Kengdenongshe Au–Ag–Pb–Zn polymetallic deposit, a newly discovered large-scale polymetallic deposit in the southeastern section of the East Kunlun Orogen (EKO), contains an Au resource of 40 t, Ag resource of 690 t and Pb–Zn resource of 10.5×10^5 t. The ore-bearing rocks are mainly composed of laminar barite and rhyolitic tuff. In this study, LA-ICP-MS zircon U–Pb dating and whole rock major and trace elements analyses have been conducted on the ore-bearing rhyolitic tuff. LA-ICP-MS zircon U–Pb dating data show that these rhyolitic tuffs were emplaced at ca. 243.3 ± 1.6 Ma. The samples show similar features to those of S-type granites, including high contents of SiO_2 (76.4–82.6 wt. %) and Al_2O_3 (11.0–12.7 wt. %) and relatively low concentrations of Na_2O (0.35–2.43 wt. %) and CaO (0.095–0.124 wt. %), with high A/CNK (molar [Al_2O_3/(CaO + Na_2O + K_2O)]) (1.72–2.03) and K_2O/Na_2O ratios (1.41–17.1). Further, they exhibit depletion in HFSEs (High Field Strength Elements) and enrichment in LREEs (Light Rare Earth Element) with negative Eu anomalies (Eu/Eu* = 0.51–0.64). These geochemical characteristics indicate that the Kengdenongcuo rhyolitic tuff originated from the fluid-absent melting of a plagioclase-poor, clay-rich metapelitic source and experienced minor fractional crystallization. In combination with arc-type magmatism and contemporaneous syn-collision granitoids in the region, the Kengdenongcuo tuff formed in a continental collision setting, implying that the Bayan Har–Songpan Ganzi Terrane collided with the East Kunlun Terrane and the Paleo-Tethys Ocean was closed at the period of ~243 Ma. The Kengdenongcuo polymetallic deposit formed at about the same time.

Keywords: Eastern Kunlun Orogen; Kengdenongshe Polymetallic Deposit; ore-hosting rhyolitic tuff; Paleo-Tethys Ocean; SEDEX

1. Introduction

The East Kunlun Orogen (EKO) has been recognized to have been formed via the collision between the Qaidam Block and the Qiangtang or Bayanhar Terrane resulting from the closure of the Paleo-Tethyan Ocean [1–5]. The EKO is also one of the important metallogenic provinces in China, including occurrences of porphyry, skarn, orogenic and sedimentary exhalative (SEDEX) type

ore deposits, most of which are associated with Early Paleozoic and Late Paleozoic-Early Mesozoic composite orogenic processes [6–11]. Previous research in this area has mostly focused on single aspects such as tectonic evolution, magmatism, mineralization and resource potential evaluation, as well as specific studies of individual ore deposits [12–17]. However, research on mutual-relationship relationship between the deep-kinetic mechanism of the orogenic process and mineralization remains weak.

The newly discovered Kengdenongshe polymetallic deposit in Maduo County, Qinghai Province, is located in the eastern segment of the EKO. Its ore has been divided into two main types of barite-type gold polymetallic mineralization and rhyolitic tuff-type Pb–Zn mineralization [18]. The ore-bearing rock is mainly composed of laminar barite and rhyolitic tuff. However, the relationship between polymetallic deposits and magma sources of mineralization-related rocks in the study area has rarely been discussed. In this study, LA-ICP-MS (Laser ablation inductively coupled plasma mass spectrometry) zircon U–Pb dating establish the time of emplacement. Whole rock major and trace elements of ore-bearing rhyolitic tuff have been conducted to reveal the petrogenesis of these rocks. This work provides more evidence for discussion on the relationship between deep-kinetic mechanisms of the orogenic process and mineralization in the eastern segment of the EKO.

2. Geological Setting and Sampling

2.1. Regional Geology

The EKO, situated in the northern part of the Qinghai-Tibet Plateau, is bounded by the Qaidam Basin to the north and the Bayan Har–Songpan Ganzi Terrane to the south (Figure 1a). It comprises the North East Kunlun Terrane (NEKT), Central East Kunlun Terrane (CEKT) and South East Kunlun Terrane (SEKT) (Figure 1b), which have been separated by the North East Kunlun Fault (NEKF), the Central East Kunlun Fault (CEKF) and the South East Kunlun Fault (SEKF), respectively.

The Kengdenongshe polymetallic deposit, situated at the southeastern part of the EKO, is located in the junction of the NEKT and SEKT (Figure 1c). Upper Proterozoic to Cenozoic strata have been exposed in the Kengdenongshe area. The Precambrian strata are mainly distributed in the central and northern parts of the region, including the Paleoproterozoic Jinshuikou Group (composed of schist, marble, gneiss and a set of amphibolites); the Mesoproterozoic Xiaomiao and Kuhai Groups (amphibolite and schist) and the Neoproterozoic Wangbaogou Group (marine intermediate-basic volcanic rock, carbonate rock and metamorphic clastic rock). The Paleozoic strata are mainly developed in the region and mostly distributed in the central and western parts of the region, including the Ordovician-Silurian Nachitai Group (comprising basaltic andesite, dacite, rhyolite and turbidites), the Devonian Yakshan Formation (millennium rock, phyllite and carbonaceous slate), the Lower Carboniferous Halaguole Formation, the Upper Carboniferous-Permian Haoteluowa Formation and the Permian Shuweimenke, Maltese and Gequ Formations (medium-felsic volcanic rocks, glutenite, limestone and slate). The Mesozoic strata, including the Lower-Middle Triassic Longwuhe, Liuchuan and Wucangjiangou Formations; the Upper Triassic Elashan Formation; and the Lower-Middle Jurassic Yangqu Formation, are mainly distributed in the middle, north, east and southwest of the area. They are dominated by sandstone, siltstone and limestone. The Cenozoic strata are mainly composed of glutenite and landslides. The fold structure of the area is developed with a predominant EW axial direction. The regional CEKF traverses the whole area, striking NWW. In addition, a large number of secondary faults with NWW, EW and NW directions are developed (Supplementary Figure S1).

There are three stages of intrusive rocks: (1) The Permian intrusive rocks include the Tolonaiqing intrusion in the south of the CEKF and the Jiadehei intrusion in the north of CEKF, which consist of granodiorite and granite, with minor diorite and tonalite; (2) The Late Triassic intrusive rock, distributed in the north of the CEKF, is represented by the Lawo tonalite intrusion. (3) The Yanshanian intrusive rock, spread across the northern part of the area, mainly consists of granite and monzonitic granite. Additionally, three main stages of volcanic rocks were developed in this area: (1) The volcanic rocks of the Mesoproterozoic Wanbaogou rock group comprise basic lava, with a small amount of

medium-basic volcanic rocks and diabase dykes; (2) The volcanic rocks of the Permian Buqingshan rocks mainly are composed of medium-sized volcanic rocks with a small amount of medium-acid volcanic rocks, which have undergone low greenschist facies metamorphism; and (3) The volcanic rocks of Triassic Hongshuichuan and Elashan Formations, which are dominated by acid lava and a small amount of volcanic agglomerates and breccia at the bottom.

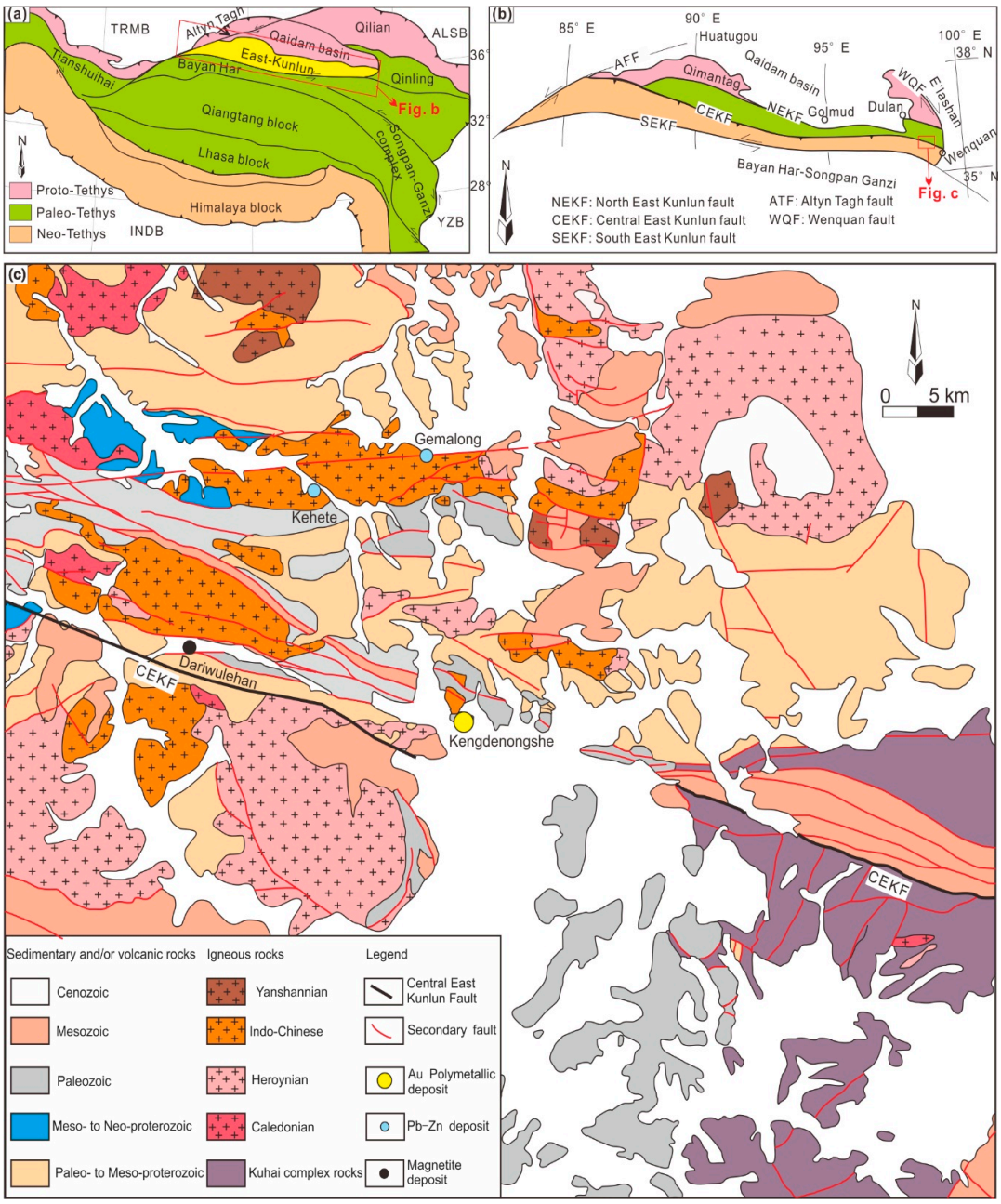

Figure 1. Tectonic outline of the (**a**) Qinghai–Tibetan Plateau, (**b**) East Kunlun Orogen (modified after Reference [19]) and (**c**) simplified geological map of the Kengdenongshe area, the eastern segment of the East Kunlun Orogen (modified after Reference [20]).

2.2. Geology of Kengdenongshe Deposit

The exposed strata in the mining area include the Paleoproterozoic Jinshuikou Group, the Late Carboniferous Haoteluowa Formation and the Early Permian Maerzhen Formation (Figure 2a). The Paleoproterozoic Jinshuikou Group was mainly distributed in the northern part of the mining area and is composed of plagiogneiss. The Late Carboniferous Haoteluowa Formation, mainly distributed in the southern part of the mining area, consists of a series of coastal-shallow marine sedimentary, clastic-carbonate and medium-basic volcanic rocks, which are the main ore-bearing strata. The Early Permian Maerzheng Formation, mainly distributed in the center of the mining area, is composed of andesite, rhyolite tuff, siliceous rock, barite rock and limestone from north to south, containing thin layered slate and dolomitic limestone, of which rhyolite tuff and barite are the main ore-bearing strata in this area. The main structure in the mining area is a NWW-oriented anticline and NW-oriented fault. The main intrusion is composed of quartz porphyry and granite porphyry, intruding into the Hongshuichuan Formation in the central the mining area. The volcanic rocks are the pyroclastic rocks of the Maerzheng Formation.

The ore body is characterized as layered, lenticular and vein-like. The length of a single ore body is generally 80–400 m with an average thickness of 4.0 to 20.5 m and maximum thickness of a single project is 47 to 155 m. The ore body mainly occurs in the rhyolitic tuff in the upper part of the limestone or/and near the interface with the limestone and in the limestone (Figure 2b,c). The features of main ore body are as follows:

V-Au–Pb–Zn–Ag ore body: This ore body is mainly developed in the interface between the rhyolitic tuff and the limestone. The ore body displays layered, expansive and branched structures with a length of 400 m and average thickness of 27.6 m. The ore body shows mineralization zoning along strike and tendency. The ore body is layered as Pb, Zn–Au, Pb, Zn, Ag–Pb and Zn from top to bottom and Au, Pb, Zn–Pb, Zn–Au and Pb from west to east. The average grade of Au, Pb and Zn is 1.5×10^{-6}, 0.68% and 1.33%, respectively (Figure 2b).

III-Pb–Zn ore body: This ore body present in the rhyolitic tuff. The ores are characterized as layered with a length of 400 m and average thickness of 29.2 m. The ore body show an inclination of 35° on the 04 line and inclination of 60° to 65°on east and west sides of the 04 line. The average grades of Pb and Zn are 1.31% and 1.42%, respectively (Figure 2c).

He (2014) [18] has divided the ore into two main types of barite-type gold polymetallic mineralization and rhyolitic tuff-type Pb–Zn polymetallic mineralization. The barite-type gold polymetallic mineralization is mainly produced in the interlayer fracture contact zone of the volcanic rock of the Maerzheng Formation and the limestone of the Haoteluo group and their tectonic fractures (Figure 3a). The ore-bearing rock is laminar barite and is layered, lenticular and contains a small number of veins (Figure 3b–d). The rhyolitic tuff-type Pb–Zn polymetallic mineralization is mainly produced in the upper plate of the barite-type ore body. The ore-bearing rock is mainly composed of rhyolitic tuff (Figure 3e,f). In this study, the samples were collected from drilling (No. ZK3501). They are classified as ore-hosting rhyolitic tuff and characterized by tuffaceous and a massive structure (Figure 3e,f). The rhyolitic tuff consists of crystal phenocrysts (~25%; plagioclase and K-feldspar), lithic clasts (~40%; irregular rhyolite and breccia) and vitric clasts (~20%; fine-particulate felsic minerals) with a small number of volcanic breccia (>2 mm; ~15%). Plagioclase has experienced weak sericitization and kaolinization, K-feldspar has undergone kaolinization and the lithic clasts have experienced chloritization.

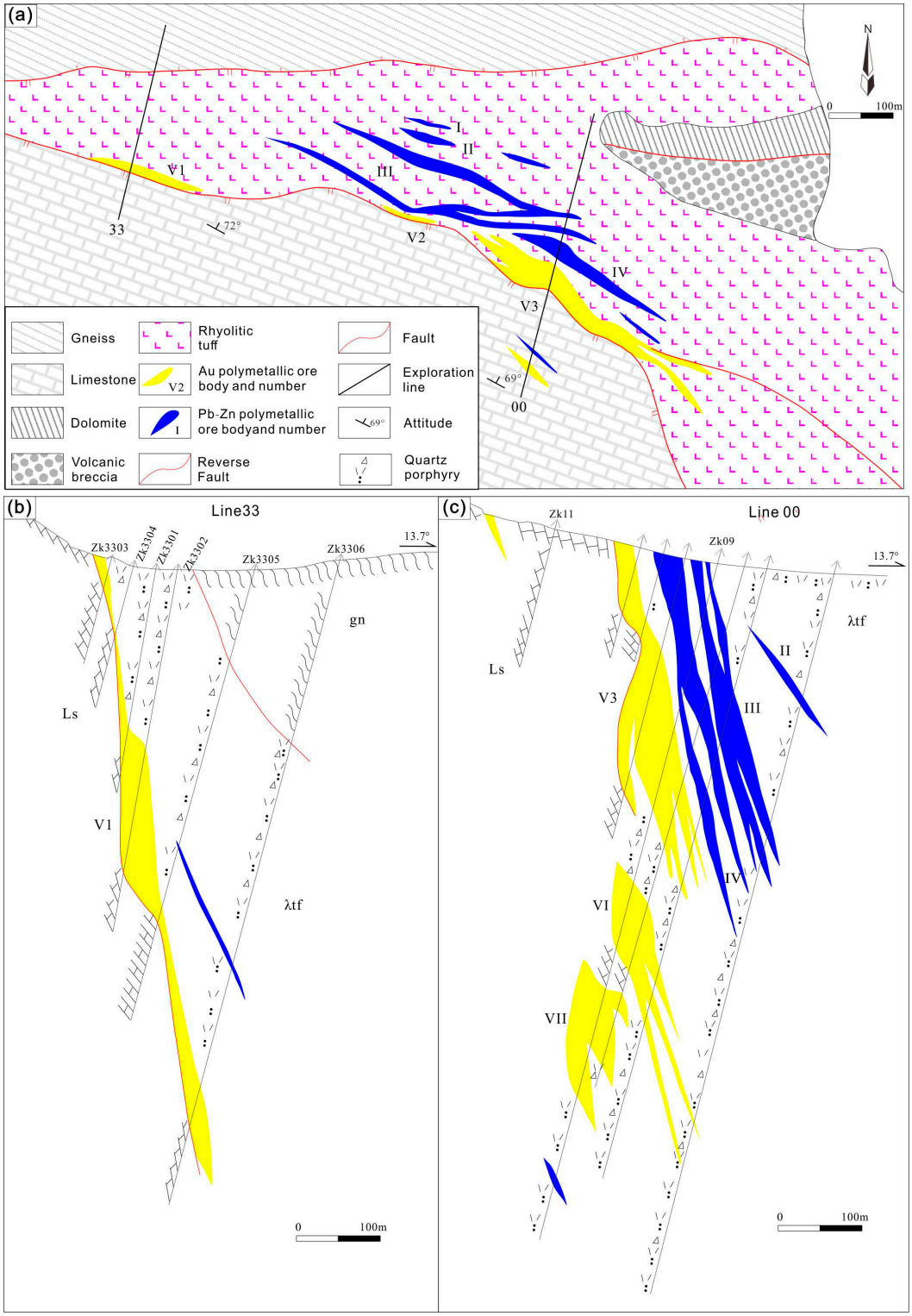

Figure 2. (**a**) Geological map, geological cross sections along exploration lines (**b**) No. 33 and (**c**) No. 00 of the Kengdenongshe polymetallic deposit (modified after Reference [14]). Ls: Limestone; λtf: Rhyolitic tuff; gn: gneiss. II: Number of ore body.

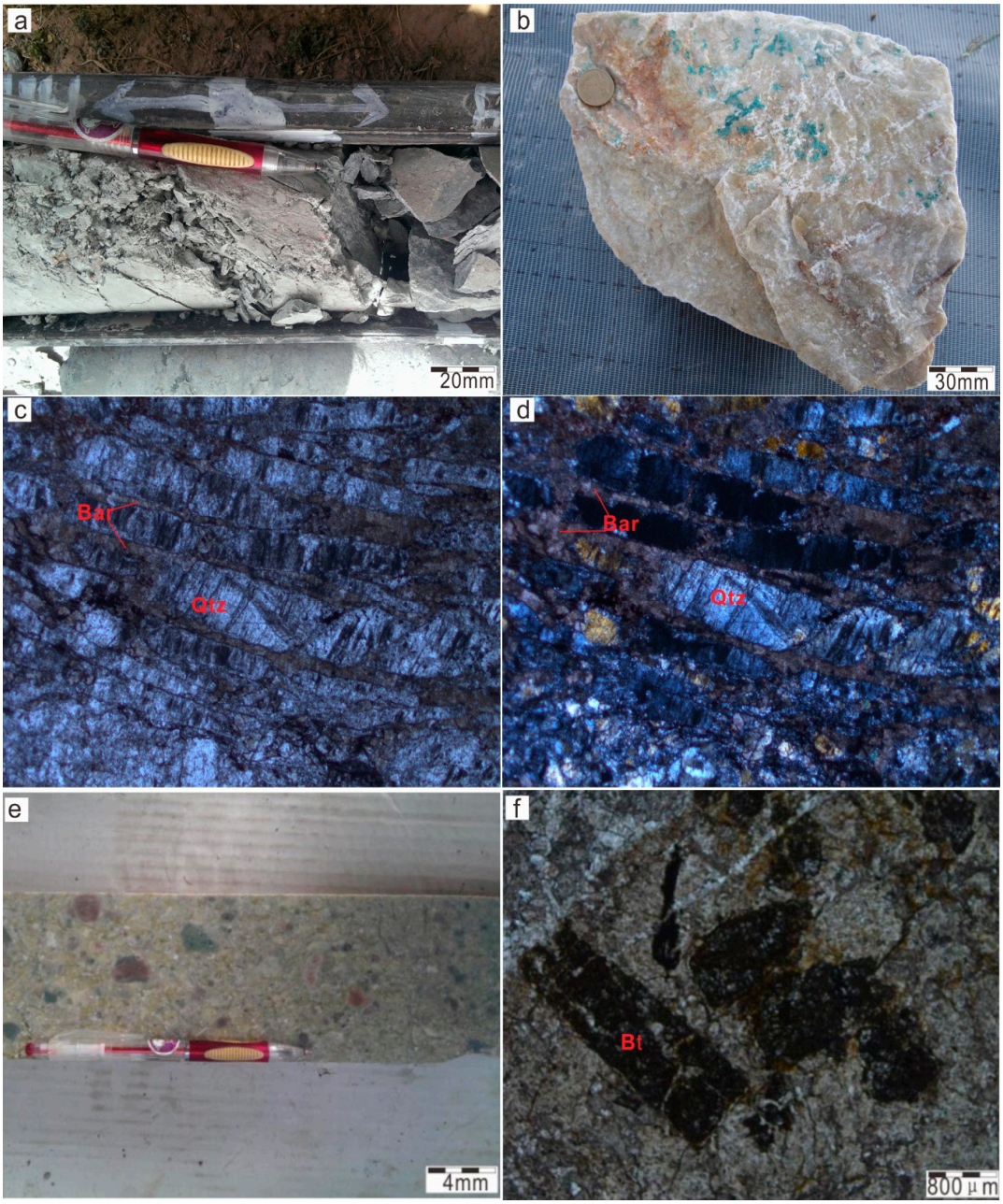

Figure 3. Petrographic photo of ore-hosting rocks in the Kengdenongshe polymetallic deposit. (**a**) field photos of ore-hosting fractured zone and (**b**) ore-hosting barite; (**c**) photomicrographs under plane-polarized light and (**d**) cross-polarized light of quartz-bearing barite veins; (**e**,**f**) photomicrographs of ore-hosting rhyolitic tuff. Bar: barite; Bt: biotite; Py: Pyrite; Qtz: Quartz.

3. Analytical Methods

3.1. LA-ICP-MS Zircon U–Pb Dating

Cathodoluminescence (CL) imaging of zircon has been taken on a JXA-880 electron microscope at the Institute of Mineral Resources, China Academy of Geological Science (IMR-CAGS), Beijing, China, to select suitable positions of zircon crystals for in-situ measurements. LA-ICP-MS zircon U–Pb dating was conducted at the IMR-CAGS. The operating conditions and data reduction processes are described in Reference [21]. Argon and helium were used to remove common Pb remaining in the gas path. The zircon GJ-1 was used as an external standard for determining sample zircons $^{206}Pb/^{238}U$ ages

(610 ± 1.7 Ma [22]) and concentrations of U, Th and Pb were measured based on known concentrations of the zircon standard M127 (U = 923 ppm, Th = 439 ppm and Th/U = 0.475 [23]). ICPMS-DataCal software (7.6, China University of Geosciences, Wuhan, China) was used to select off-line raw data, analyze signals and quantitatively calibrate for U–Pb dating [24]. Concordia diagrams and weighted mean calculations were made with Isoplot/Ex ver3 (Version 3.0, School of resources and environment, Yangtze University, Jinzhou, China). The uncertainty for each individual analysis is quoted at the 2σ level and errors on weighted-mean ages are shown at the 95% confidence level.

3.2. Whole-Rock Major and Trace Elements Analyses

Whole rock samples were powdered to 200-mesh size for analysis of major and trace element compositions of bulk-rock samples. Whole rock major and trace elements were determined at the analytical laboratory of Beijing Research Institute of Uranium Geology, Beijing, China. Major elements were analyzed through X-ray fluorescence. The precision on standards was better than 2%. Trace elements were determined through inductively coupled plasma mass spectrometry (ICP-MS; Agilent 7500a) (Agilent, Technologies, Santa Clara, CA, USA). Standard materials G2 and GSR-1 were used for reference. The detailed sample-digesting procedure for ICP–MS analyses and analytical precision and accuracy for trace elements are described in Reference [25].

4. Results

4.1. Zircon U–Pb Age

The sample of rhyolite tuff (13KDNS-1) was used to determine the zircon U–Pb isotopic age. The analyzed zircon was colorless, medium in size (50–110 um) and had euhedral to subhedral prismatic structure with oscillatory zoning (Figure 4a). Zircons from this area show high contents of Th (125–659 ppm) and U (165–916 ppm) and high Th/U ratios (0.47–0.90) (Table 1). The chondrite-normalized REE diagram of these zircons displays positive Ce anomalies and HREE (Heavy Rare Earth Elements) enrichments (Supplementary Table S1 and Figure S2). These features indicate that these zircons crystallized from magma [26,27]. Eleven zircons yielded a $^{206}Pb/^{238}U$ weighted mean age of 243.3 ± 1.6 Ma (n = 11, MSWD = 0.12) (Figure 4b), which represents the formation age of the rhyolite tuff.

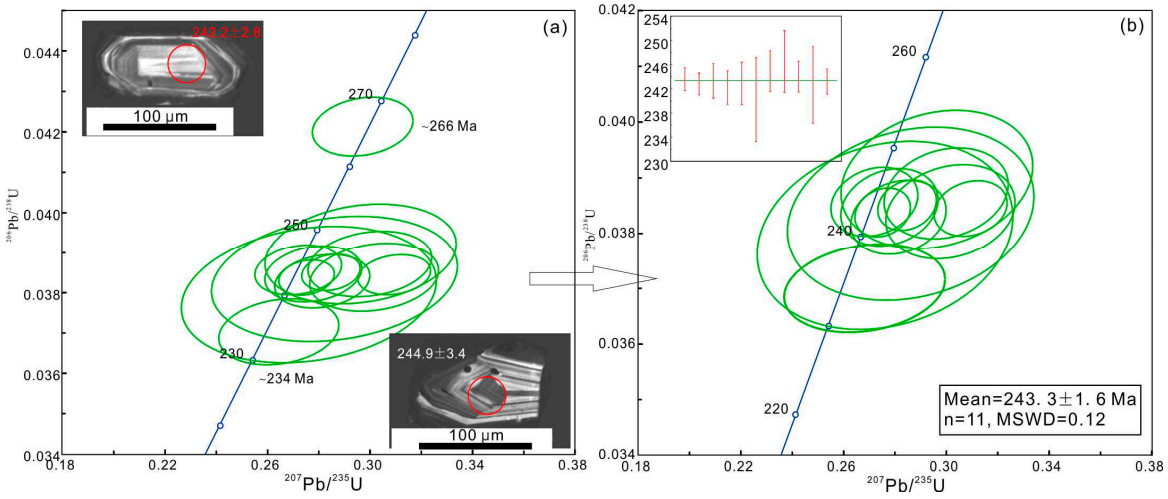

Figure 4. (**a**) Cathodoluminescence (CL) images and (**b**) concordia diagrams for zircons from the Kendenongshe rhyolitic tuff. Red circles represent the locations of LA–ICPMS U–Pb dating.

Table 1. Zircon LA-ICP-MS U–Pb data of the ore-hosting rhyolitic tuff in the Kendenongshe polymetallic deposit.

Spot	Concentrations (ppm)				Isotopic Ratios								Isotopic Age (Ma)			
	Pb*	Th	U	Th/U	$^{207}Pb/^{206}Pb$	±1δ	$^{207}Pb/^{235}U$	±1δ	$^{206}Pb/^{238}U$	±1δ	$^{208}Pb/^{232}Th$	±1δ	$^{207}Pb/^{235}U$	±1δ	$^{206}Pb/^{238}U$	±1δ
KDNS-2-2-01	37	227	480	0.47	0.0524	0.0025	0.2778	0.0125	0.0385	0.0005	0.0134	0.0004	249	10	243	3
KDNS-2-2-10	51	659	916	0.72	0.0533	0.0024	0.2813	0.0123	0.0383	0.0004	0.0118	0.0002	252	10	242	3
KDNS-2-2-13	31	153	298	0.51	0.0570	0.0033	0.3016	0.0166	0.0384	0.0006	0.0133	0.0004	268	13	243	4
KDNS-2-2-18	52	347	457	0.76	0.0528	0.0064	0.2761	0.0329	0.0380	0.0011	0.0129	0.0009	248	26	240	7
KDNS-2-2-19	16	259	288	0.90	0.0562	0.0031	0.2999	0.0159	0.0387	0.0005	0.0122	0.0003	266	12	245	3
KDNS-2-2-22	21	323	395	0.82	0.0512	0.0023	0.2971	0.0130	0.0421	0.0005	0.0131	0.0003	264	10	266	3
KDNS-2-1-03	26	188	398	0.47	0.0552	0.0047	0.2963	0.0246	0.0390	0.0008	0.0123	0.0006	264	19	247	5
KDNS-2-1-15	41	444	581	0.77	0.0511	0.0022	0.2720	0.0112	0.0386	0.0004	0.0119	0.0002	244	9	244	3
KDNS-2-1-16	48	433	776	0.56	0.0518	0.0031	0.2644	0.0155	0.0370	0.0005	0.0116	0.0004	238	12	234	3
KDNS-2-1-17	13	125	165	0.76	0.0541	0.0061	0.2861	0.0317	0.0384	0.0010	0.0116	0.0006	256	25	243	6
KDNS-2-1-20	43	416	792	0.52	0.0584	0.0019	0.3094	0.0094	0.0385	0.0003	0.0119	0.0002	274	7	243	2

Pb* = Total Pb.

4.2. Whole-Rock Geochemical Components

Rhyolite tuff had high contents of SiO_2 (76.43–82.62 wt. %) and $Na_2O + K_2O$ (5.25–6.38 wt. %) (Table 2), belonging to granite (Figure 5a). In the K_2O versus SiO_2 diagram, the data plotted in the field of medium-high K series (Figure 5b). In the plot of ^{T}FeO–$Na_2O + K_2O$–MgO, the data plot as calc-alkaline (Figure 5c). The samples also have low contents of MgO (0.59–0.75 wt. %) and TiO_2 (0.05–0.08 wt. %) but high contents of Al_2O_3 (9.21–12.74 wt. %). In the A/CNK versus A/NK diagram, the data show peraluminous features (Figure 5d). However, the Al_2O_3 compositions of the samples (11.0–12.7 wt. %), except for one sample (9.2 wt. %), show as weakly peraluminous rocks. These samples display negative Eu anomalies (Eu/Eu* = 0.51–0.64) and LREE (Light Rare Earth Element) enrichment ($(La/Yb)_N$ = 14.5–17.7) (Figure 6a). The primitive mantle normalized diagram of studied samples displays depletion in HFSEs (high-field strength elements, namely Nb and Ta) (Figure 6b).

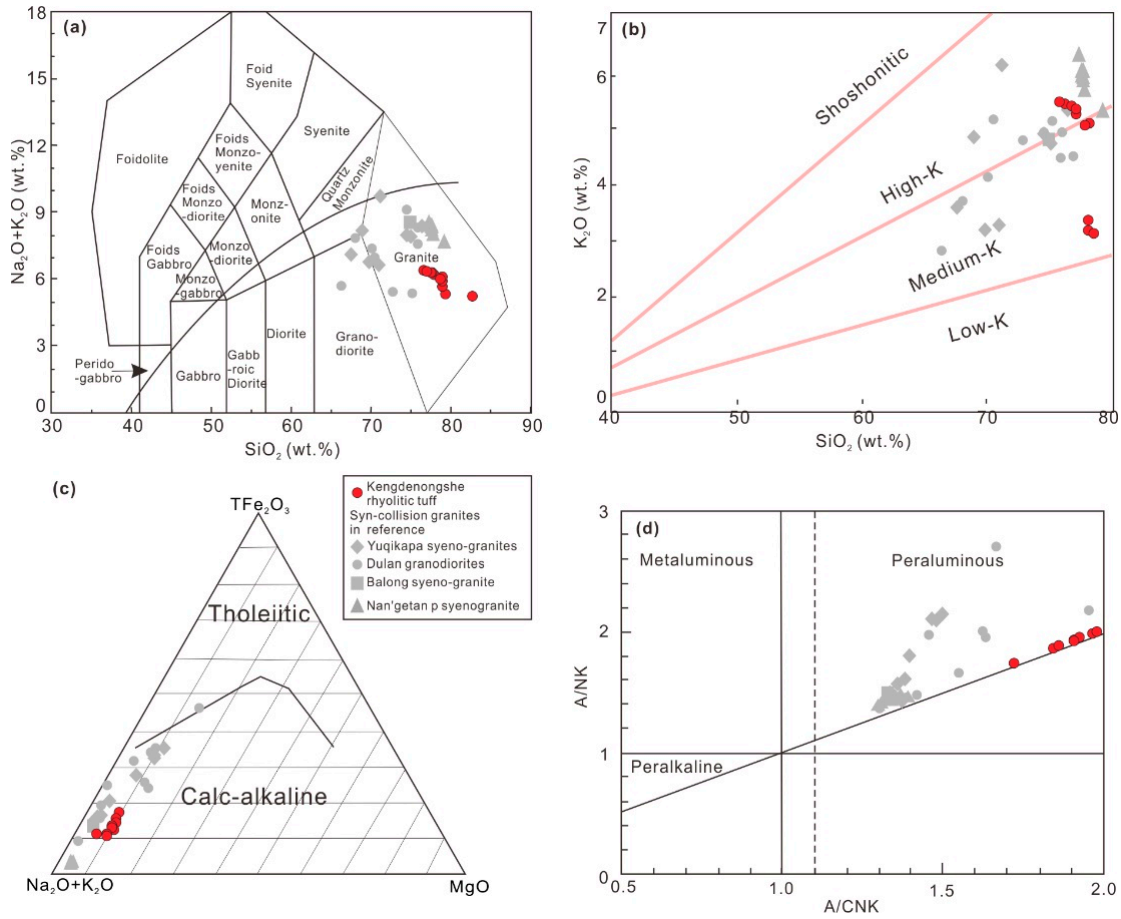

Figure 5. (**a**) Total alkalis versus SiO_2 diagram [28]; (**b**) K_2O vs. SiO_2 discrimination diagram [29]; (**c**) AFM diagram (after Reference [30]); (**d**) A/CNK versus A/NK diagram [31]. Data of Dulan granodiorites in the NEKO were taken from Reference [32]; Nan'getan syenogranites in the NEKO were taken from Reference [33]; Balong syenogranite in the transition between the CEKO and SEKO were taken from Reference [34]; Yuqikapa syenogranites in West Kunlun were taken from Reference [35].

Table 2. Whole rock major and trace element data of the ore-hosting rhyolitic tuff in the Kendenongshe polymetallic deposit.

Sample	KD2-1	KD2-2	KD2-3	KD2-4	KD2-5	KD2-6	KD2-7	KD2-8	KD2-9	KD2-10	KD2-11	KD2-12
SiO_2	78.84	77.74	77.5	76.43	76.84	77.4	77.77	78.53	82.62	78.78	79.21	78.78
TiO_2	0.075	0.062	0.064	0.067	0.058	0.071	0.054	0.069	0.026	0.073	0.072	0.056
Al_2O_3	11.4	11.8	12.1	12.7	12.4	12.3	12.0	11.6	9.2	11.6	11.0	11.4
FeO	0.250	0.590	0.300	0.510	0.360	0.310	0.340	0.370	0.280	0.200	0.380	0.210
Fe_2O_3	0.572	0.707	0.676	0.702	0.722	0.714	0.669	0.627	0.426	0.648	0.893	0.804
MnO	0.007	0.007	0.005	0.005	0.007	0.007	0.008	0.008	0.004	0.006	0.005	0.004
MgO	0.63	0.68	0.676	0.745	0.703	0.749	0.685	0.668	0.371	0.616	0.59	0.608
CaO	0.097	0.124	0.096	0.106	0.102	0.1	0.102	0.096	0.1	0.112	0.099	0.095
Na_2O	0.491	0.347	0.348	0.352	0.362	0.364	0.416	0.417	2.31	2.46	1.93	2.01
K_2O	5.61	5.89	5.94	6.03	5.99	5.95	5.78	5.57	2.94	3.47	3.41	3.66
P_2O_5	0.015	0.02	0.023	0.025	0.024	0.013	0.019	0.024	0.012	0.019	0.02	0.019
LOI	1.81	2.12	2.08	2.39	2.3	1.9	1.91	1.8	1.38	1.71	2.21	2.08
Total	99.8	100.1	99.8	100.1	99.8	99.8	99.8	99.8	99.7	99.7	99.9	99.7
Li	7.77	10.4	7.27	7.02	9.18	8.45	10.9	10.9	15.5	12.1	12.1	11.4
Be	0.856	1.02	1.25	0.84	1.08	1.01	1.09	0.987	0.819	0.996	0.967	0.945
Sc	3.32	3.84	4.05	3.96	3.8	3.8	3.8	3.88	2.9	3.73	3.8	3.71
V	6.63	5.8	5.25	5.71	8.07	8.89	7.51	6.83	5.23	4.79	6.4	5.8
Cr	1.82	2.74	3.73	3.5	0.59	1.36	1.57	0.909	0.987	1.44	0.781	2.65
Co	0.135	0.132	0.141	0.206	0.104	0.119	0.107	0.112	0.165	0.1	0.084	0.113
Ni	0.86	0.917	0.929	1.32	0.428	1.11	0.937	0.541	0.82	0.802	0.519	1.61
Cu	24.3	42.4	37.5	36	42.3	29.6	33.5	31.4	54.8	36.5	53.6	47.2
Zn	61.4	105	114	117	122	73.3	78.4	78.4	114	84.4	108	89.5
Ga	15.4	17.2	17.5	17.5	17	18	16.8	17.3	11.5	14.8	15.3	15.4
Rb	177	197	194	195	195	205	195	197	92.2	131	130	133
Sr	44.8	58.2	65.1	63.6	64.3	53.7	55.4	50.4	63.2	58.2	52	61.3
Y	12.2	11.6	11.6	11.3	11.3	11.4	12.3	12.4	10.3	10.1	11.2	10.9
Zr	89.6	93.2	91.5	91.1	92.5	99.9	95.9	99	72.5	92.8	94.1	91.1
Nb	11.1	11.7	12.1	12	11.9	11.9	11.7	11.9	8.57	11	11.5	11.7
Mo	1.42	6.02	3.22	2.2	3.14	1.56	2.08	2.51	1.01	0.531	1.31	0.807
Cd	0.396	0.22	0.188	0.19	0.174	0.382	0.266	0.289	0.382	0.402	0.343	0.355
In	0.022	0.019	0.024	0.02	0.025	0.014	0.023	0.02	0.028	0.017	0.027	0.021
Sb	3.46	4.79	4.2	4.31	4.6	4.15	4.42	4.14	264	5.02	6.92	6.1
Cs	1.61	2.05	2.03	2.05	1.92	1.86	1.74	1.84	1.3	2.38	2.52	2.38
Ba	2610	3689	3925	3333	4833	3367	4187	3000	5875	2785	2777	4698
Hf	3.1	3.32	3.18	3.19	3.19	3.34	3.34	3.54	2.47	3.15	3.22	3.09
Ta	1.02	1.05	1.02	1.05	1.05	1.06	1.03	1.14	0.799	0.912	0.959	1.1
W	1.31	1.48	1.39	1.5	1.37	1.5	1.44	1.4	1.98	1.59	1.75	1.81
Re	0.005	0.009	0.02	<0.002	0.012	0.02	0.009	0.015	0.014	0.004	0.01	0.007
Tl	13.3	14.9	14.6	14.3	13.9	14	14.2	14.3	10.7	13.2	14.1	14.4
Pb	118	380	402	427	412	125	162	199	278	85	364	148
Bi	0.316	0.328	0.333	0.316	0.327	0.302	0.299	0.328	0.267	0.259	0.302	0.331
Th	13.7	15.3	15.3	14.9	14.7	15.3	14.5	15.3	12.4	13.5	14.4	14.6
U	3.75	3.6	3.68	3.44	3.38	3.68	3.52	3.84	2.02	2.26	2.66	2.78
La	32	34.8	35.2	34.4	34.2	36.1	34.2	35.6	29.7	31	32.6	34
Ce	55.5	60	60.8	59.9	59.2	62.9	59.2	62.1	51.4	54.2	56.5	58.1
Pr	5.79	6.24	6.28	6.19	6.13	6.52	6.11	6.36	5.17	5.56	5.76	5.97
Nd	19.3	20.7	21	20.4	20.2	21.8	20.5	21.2	16.9	18.4	19	19.8

LOI: Loss on ignition.

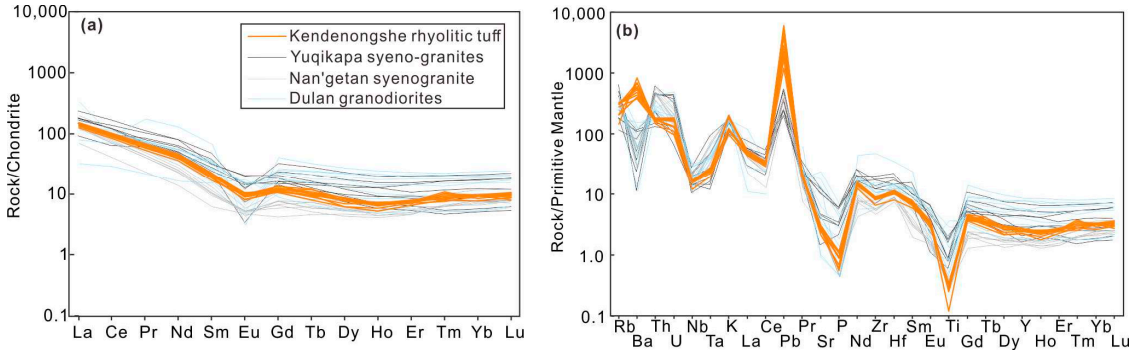

Figure 6. (**a**) The chondrite-normalized REE contents and (**b**) primitive mantle-normalized immobile trace element content diagrams for the Kendenongshe rhyolitic tuff. Data source: the OIB and N-MORB lines were taken from Reference [31]; Dulan granodiorites in the NEKO were taken from Reference [32]; Nan'getan syenogranite in the NEKO were taken from Reference [33]; Yuqikapa syenogranites in West Kunlun were taken from Reference [35].

5. Discussion

5.1. Petrogenesis of Kengdenongshe Rhyolitic Tuff

The petrography of the biotite phenocryst of the Kengdenongshe rhyolitic tuff shows evidence of alteration (Figure 3), which also has been supported by relatively high LOI content of 1.38–2.39 wt. % (Table 2). However, there is no significant correlation among LOI and Al_2O_3, CaO, Na_2O and K_2O (Supplementary Figure S3). Thus, the alteration displayed is considered as insignificant concerning the interpretation of the magmatic evolution.

The samples in this study display A/CNK > 1 (molar [Al_2O_3/(CaO + Na_2O + K_2O)]) and K_2O/Na_2O > 1 and plot in the fields of high-K, calc-alkaline and peraluminous rocks (Figure 5b–d), which is similar to the relationships of typical S-type granites. S-type granites are characterized by high SiO_2 compositions, relatively low Na_2O and CaO contents and high A/CNK ratio (>1.1) [36–42] (Figure 7a). Petrography reveals that the Kengdenongshe rhyolitic tuff comprises biotite with an absence of alkaline-rich ferro-magnesian minerals, which is consistent with S-type and/or highly fractionated I-type granites [41,42] (Figure 3). Thus, these geochemical and mineralogical features of the Kengdenongshe rhyolitic tuff are similar to characteristics of S-type granites.

It has been proved that both highly fractionated I-type and S-type granites would yield the geochemical and mineralogical features above [37,42]. Highly fractionated granites always display decreasing Zr contents and Zr/Hf and Nb/Ta ratios with increasing fractional crystallization [43–45]. Although Kengdenongshe rhyolitic tuffs have high SiO_2 contents (>73 wt. %) that resemble highly fractionated granites [42,46–49], they also exhibit relatively high Zr contents (73–100 ppm) and high Zr/Hf ratios (28.0–29.5). Moreover, in the plot of Rb–Ba–Sr, samples in this study fell into the field of normal granites rather than highly differentiated granites (Figure 7b). Thus, we propose that Kengdenongshe rhyolitic tuff originated from primary partial melting of a source with minor fractionation [50–53].

Peraluminous intermediate to felsic melts (SiO_2 = 70.7–74.8 wt. %, A/CNK = 1.18–1.31; K_2O/Na_2O = 1.33–1.76), could likely originate from dehydration melting of amphibolite or from partial melting of metaluminous protoliths (namely amphibolites and felsic orthogneisses) at low melting fractions and anhydrous conditions [54,55]. However, Kengdelongcuo rhyolitic tuff has higher SiO_2 content (76.8–82.6 wt. %), A/CNK (1.84–2.03) and K_2O/Na_2O (1.27–17.13) ratios than these peraluminous melts, which are also inconsistent with the melts from meta-igneous protoliths [56]. Alternatively, peraluminous granitoids likely derived from the partial melting of metasedimentary protoliths, such as clay-rich metapelites and clay-poor metagraywackes [40,41,56–59]. Kengdenongshe rhyolitic tuff shows high SiO_2 content, strongly peraluminous characteristics and high K_2O/Na_2O

ratios, which are similar to the melts from a metasedimentary source [56]. The samples studied are characterized by low CaO/Na_2O ratios (<0.3) and low ^{T}FeO + MgO + TiO_2 contents (mostly < 2 wt. %), demonstrating that these strongly peraluminous granites were sourced from partial melting of a metapelitic source [55] (Figure 7c,d).

Additionally, experimental study and modelling have proved that some trace element contents and/or its ratios could be used to highlight the melting modes of muscovite and plagioclase in the metapelites source [50,51]. Melts derived from fluid-fluxed melting, consume more plagioclase than muscovite, show high Sr and low Rb contents and low Rb/Sr ratios. On the contrary, melts derived from fluid-absent melting, consume more muscovite than plagioclase, have low Sr and high Rb contents and high Rb/Sr ratios [60]. The Kendenongshe tuff has very high K_2O (2.94–6.03 wt. %), high Rb (130–205 ppm) and low Sr (45–65 ppm) compositions along with high Rb/Sr ratios (1.46–3.95) and highly fractionated REE patterns (Figure 6a). In addition, the samples studied show negligible Eu anomalies and Sr depletion (Figure 6), which may be produced by the occurrence of minor residual plagioclase in the magmatic source. Thus, the Kengdenongcuo tuff originated from fluid-absent melting of the plagioclase-poor, clay-rich metapelitic source.

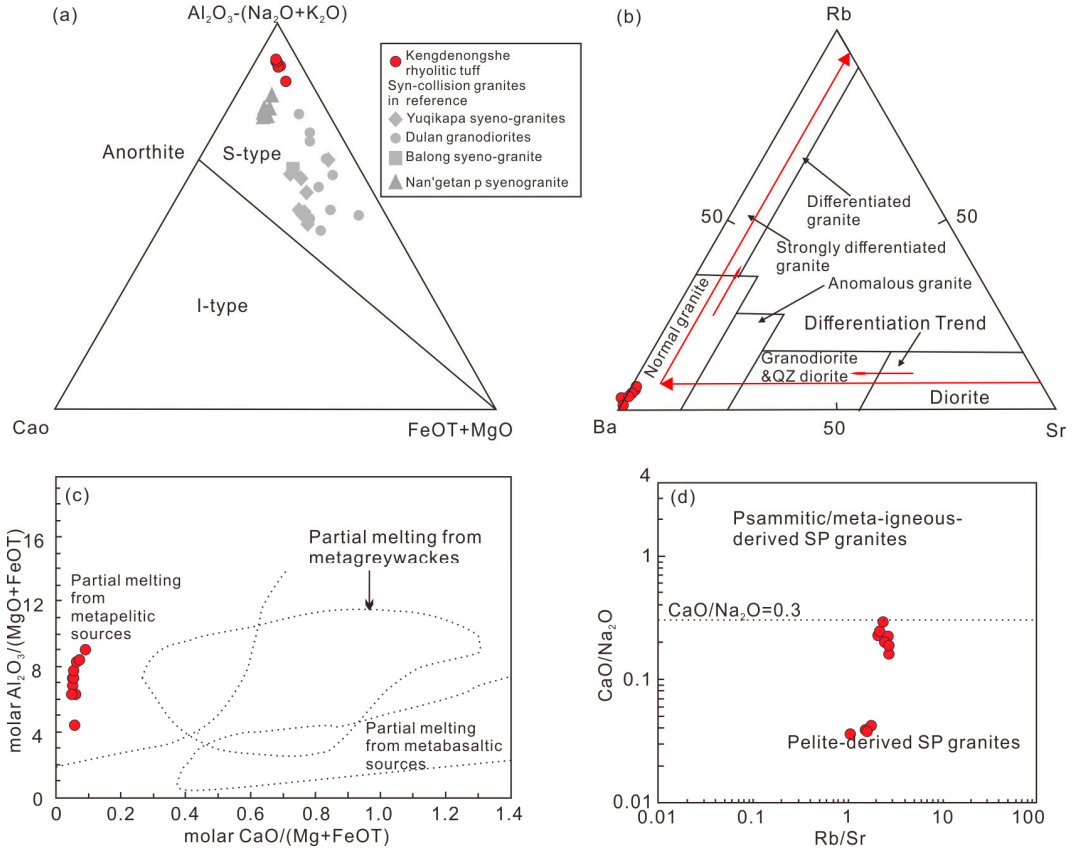

Figure 7. (**a**) (Al_2O_3–(Na_2O + K_2O))–CaO–FeO^T + MgO and (**b**) Rb–Ba–Sr diagram [61], (**c**) molar Al_2O_3/(MgO + FeO^T) vs. molar CaO/(MgO + FeO^T) diagram [62], (**d**) Rb/Sr vs. CaO/Na_2O (modified after Reference [55]).

5.2. The Geodynamic Background for the Magmatism

Previous study has shown that the EKO has experienced at least two episodes of orogenesis, which display a close relationship with the opening and closing of the Proto-Tethys Ocean and the Paleo-Tethys Ocean [63–66]. It has been assumed that the opening and spreading of the Paleo-Tethys Ocean began in the early/middle Devonian based on evidence from ophiolites and volcanic rocks in the area [64,67–71]. Subsequently, the Paleo-Tethys Ocean subducted northward beneath the EKO,

producing subduction-related granitoids (261–248 Ma of zircon U–Pb age [72–74]). However, the timing of Paleo-Tethys Ocean closure remains debated [75–77].

In the EKO, both Nan'getan granodiorites (~243 Ma) and Wulonggou granodiorite (246–248 Ma) in the NEKT show island arc-related features, including low Sr/Y and high Y and formed in an arc setting [17,78]. Haishigou volcanic lavas (244–245 Ma) in the NEKT show high-K calc-alkaline rocks, LILE enrichment and HFSE depletion, as well as high initial $^{87}Sr/^{86}Sr$ ratios and moderately negative $\varepsilon_{Nd}(t)$ values, indicating a continent-type magma source [79–81]. The Halagatu granitoid plutons (248–244 Ma) in the SEKT, characterized by high-K, calc-alkalinity and metaluminous to peraluminous areas with negative Nb–Ta and Ti anomalies, were generated in a continental arc setting [66]. Balong granodiorite and quartz-diorite (263–241 Ma) in the CEKT, characterized by the calc-alkaline series and metaluminous and enriched Sr–Nd isotopes, have been recognized to be sourced from dehydration melting of lower crustal rocks during the northward subduction of the Anyemaqen Ocean [66]. Moreover, even on the north margin of the EKO, the Kunbei granites in the southwestern Qaidam Basin (247–251 Ma) belong to highly fractionated I-type granites, forming at an active continental margin setting resulting from northward subduction of the Paleo-Tethys oceanic crust beneath the Qaidam Basin [82]. These evidences indicate a continental arc setting in this area at the period of 243 Ma ago, which was closely related to the northward subduction of the Paleo-Tethys Ocean.

Eleven zircons from the Kengdenongcuo rhyolitic tuff in this study yielded a weighted mean age of 243.3 ± 1.6 Ma (n = 11, MSWD = 0.12) (Figure 4). The Kengdenongshe tuff exhibits enrichments in LILEs and depletions in HFSEs, indicating a convergent margin setting (Figure 6). They also show similar geochemical and petrographic features typical of S-type granites, which have been proved to be formed during continental collision, with minor occurrences in continental arcs or post-orogenic settings [83]. Barbarin (1999) [84] assumed that typical S-type granites mostly originated from metasedimentary sources in the deep crust in continent-continent collision or post-collision settings. Himalayan-type strongly peraluminous granites, which are typical S-type granites, developed at the syn- and post-collisional setting with a thickened crust (>50 km) [55]. Combined with previous geochronological data, the Kengdelongcuo tuff has contemporary syn-collision magmatism in the eastern segment of the EKO. In the region, the contemporaneous granodiorites in Dulan (ca. 246–242 Ma) in the NEKO, are characterized by high K, are calc-alkaline, peraluminous and enriched in LILEs and LREEs with a strong Eu anomaly and are derived from a syn-collision setting [32]. The Nan'getan peraluminous syenogranite of the NEKO was (~240 Ma) generated in a syn-collision setting [33]. The syenogranite near the Balong region in the transition between the CEKO and SEKO (ca. 231 Ma) was produced at a higher crustal level in a syn-collisional setting [34]. Additionally, in West Kunlun, the contemporaneous Yuqikapa syenogranites (242.9 ± 2.6 Ma) also formed in a syn-collisional tectonic setting [35]. Thus, the Kengdenongshe rhyolitic tuff in this study also occurred in a syn-collisional tectonic setting.

The combination of arc-type magmatism (>243 Ma) and syn-collision granitoids (≤243 Ma) above, suggests a transformation process from subduction to syn-collision in the EKO and onset of collision related to the consumption of the Paleo-Tethys Ocean at ~243 Ma. Furthermore, a regional angular unconformity has recently been recognized between the Late-Triassic terrestrial Babaoshan and Early-Triassic shallow marine Naocangjiangou formations [71,85,86]. Contemporaneous high-pressure metamorphic events (the ~242 Ma of Jinshuikou granitic gneiss [87]) also have been found. These evidences further explain that the Bayan Har–Songpan Ganzi Terrane collided with the East Kunlun Terrane and the Paleo-Tethys Ocean was closed at the period of ~243 Ma.

5.3. Implications on Links between the Magmatism and Mineralization

The large-type Kengdenongshe polymetallic deposit is located in the eastern segment of the EKO. Due to its new discovery and shortage of research work, the genesis of the deposit remains controversial. In the Kengdenongcuo polymetallic deposit, the rhyolitic tuff-type Pb–Zn mineralization is mainly produced in the upper plate of the barite-type ore body (Figure 2). The ore-bearing rock is

mainly composed of rhyolitic tuff. Thus, this crystallization age of rhyolitic tuff (~243 Ma) also could represent the age of mineralization.

Jiang (2014) [88] assumed a telescoped porphyry-high-sulfidation epithermal deposit according to the type of mineralization. He (2014) [18] considered SEDEX-superimposed deposits according to the characteristics of the ore-hosting rock. The former discovered that quartz porphyry and granite porphyry in the mining area exhibited mineralization and that the ore structure is vein-like and vein-disseminated along with ore minerals of galena and sphalerite with a small amount of plaque. Thus, it is believed that there is porphyry mineralization before the barite-sulfide gold mineralization. However, the latter found that later-stage veins, renticular barite and pyrite veins intruded into the early-stage ore-hosting barite layer or surrounding rock, showing that the later-stage magmatic hydrothermal fluid has modified the early stage ore-hosting rock and ore body. It showed that superposition and transformation of multi-stage mineralization has occurred in the mining area. In this study, we also found: (1) barite-type gold polymetallic mineralization mainly occurred in the barite layer, which originated from hydrothermal sedimentation; and (2) thyolitic tuff-type Pb–Zn mineralization mainly occurred in rhyolite tuff, which was derived from volcanic eruptions and deposits.

6. Conclusions

(1) LA-ICP-MS zircon U–Pb dating data show that ore-bearing rhyolitic tuffs were emplaced 243.3 ± 1.6 Ma. The crystallization age of the rhyolite tuff (~243 Ma) also represents the age of mineralization in the Kengdenongshe polymetallic deposit.

(2) Kengdenongcuo rhyolitic tuff originated from fluid-absent melting of the plagioclase-poor, clay-rich metapelitic source and experienced minor fractional crystallization.

(3) Kengdenongcuo rhyolitic tuff formed in a continental collision setting, which indicates that the Bayan Har–Songpan Ganzi Terrane collided with the East Kunlun Terrane and the Paleo-Tethys Ocean closed ~243 Ma.

Supplementary Materials: The following are available online at http://www.mdpi.com/2075-163X/9/10/589/s1, Figure S1: The main sedimentary sequences of the EKOB (Modified from [89,90]), Figure S2: The chondrite-normalized REE patterns for zircons, Figure S3: Plots of LOI versus Al_2O_3, CaO, Na_2O and K_2O, Table S1: Zircon trace element data of the Kendenongshe rhyolitic tuff.

Author Contributions: Data curation, X.S., Y.M. and E.-Q.Z.; Formal analysis, Y.M., E.-Q.Z. and W.G.; Project administration, R.X.; Writing—original draft, Y.-Y.L.

Funding: This research was funded by the China Geological Survey Program (Nos. 1212011121128, 12120114083301) and National Natural Science Foundation of China (41802077).

Conflicts of Interest: The authors declare no conflict of interest.

References

1. Peter, M.; Burchfiel, B.C.; Liang, K.Y.; Zhao, Z.Y. Geomorphic evidence for active faulting in the Altyn Tagh and northern Tibet and qualitative estimates of its contribution to the convergence of India and Eurasia. *Geology* **1987**, *15*, 249–253.
2. Metcalfe, I. Gondwanaland dispersion, Asian accretion and evolution of eastern Tethys. *Aust. J. Earth Sci.* **1996**, *43*, 605–623. [CrossRef]
3. Deng, J.; Wang, Q.F.; Li, G.J.; Santosh, M. Cenozoic tectono-magmatic and metallogenic processes in the Sanjiang region, southwestern China. *Earth-Sci. Rev.* **2014**, *138*, 268–299. [CrossRef]
4. Deng, J.; Wang, Q.F.; Li, G.J.; Wang, C. Tethys tectonic evolution and its bearing on the distribution of important mineral deposits in the Sanjiang region, SW China. *Gondwana Res.* **2014**, *26*, 419–437. [CrossRef]
5. Dong, Y.P.; He, D.F.; Sun, S.S.; Liu, X.M.; Zhou, X.H.; Zhang, F.F.; Yang, Z.; Cheng, B.; Zhao, G.C.; Li, J. Subduction and accretionary tectonics of the East Kunlun orogen, western segment of the Central China Orogenic System. *Earth-Sci. Rev.* **2018**, *186*, 231–261. [CrossRef]

6. Feng, C.Y.; Li, D.S.; Wu, Z.S.; Li, J.H.; Zhang, Z.Y.; Zhang, A.K.; Shu, X.F.; Su, S.S. Major types, time-space distribution and metallogeneses of polymetallic deposits in the Qimantage metallogenic belt, Eastern Kunlun Area. *Northwest. Geol.* **2010**, *43*, 10–17. (In Chinese)
7. Du, Y.L.; Jia, Q.Z.; Han, S.F. Mesozoic tectono-magmatic-mineralization and copper-gold polymetallic ore prospecting research in East Kunlun metallogenic belt in Qinghai. *Northwest. Geol.* **2012**, *45*, 69–75. (In Chinese)
8. Xu, C.K.; Liu, S.B.; Zhao, Z.J.; Zhang, M.F.; Zhang, K.C.; Liu, J.H.; Zhan, F.Y.; Huang, C.H.; Zhang, Z.Y.; Wang, H.Y.; et al. Metallogenic law and prospect direction of Iron deposits in the East Kunlun metallogenic belt in Qinghai. *Acta Geol. Sin.* **2012**, *86*, 1621–1636. (In Chinese)
9. Deng, J.; Wang, Q.F. Gold mineralization in China: Metallogenic provinces, deposit types and tectonic framework. *Gondwana Res.* **2016**, *36*, 219–274. [CrossRef]
10. Deng, J.; Wang, Q.F.; Li, G.J. Tectonic evolution, superimposed orogeny, and composite metallogenic system in China. *Gondwana Res.* **2017**, *50*, 216–266. [CrossRef]
11. Yu, M.; Feng, C.Y.; Santosh, M.; Mao, J.W.; Zhu, Y.F.; Zhao, Y.M.; Li, D.X.; Li, B. The Qiman Tagh Orogen as a window to the crustal evolution in northern Qinghai-Tibet Plateau. *Earth-Sci. Rev.* **2017**, *167*, 103–123. [CrossRef]
12. Feng, C.Y.; Li, D.S.; Qu, W.J.; Du, A.D.; Wang, S.; Su, S.S.; Jiang, J.H. Re–Os isotopic dating of molybdenite from the Suolajier skarn-type copper–molybdenum deposit of Qimatage Mountain in Qinghai province and its geological significance. *Rock Miner. Anal.* **2009**, *28*, 223–227. (In Chinese)
13. Tian, C.S.; Feng, C.Y.; Li, J.H.; Cao, D.Z. ^{40}Ar-^{39}Ar geochronology of Tawenchahan Fe-polymetallic deposit in Qimantag Mountain of Qinghai province and its geological implications. *Miner. Depos.* **2012**, *32*, 169–176. (In Chinese)
14. Ding, Q.F.; Jiang, S.Y.; Sun, F.Y. Zircon U-Pb geochronology, geochemical and Sr-Nd-Hf isotopic compositions of the Triassic granite and diorite dikes from the Wulonggou mining area in the Eastern Kunlun Orogen, NW China: Petrogenesis and tectonic implications. *Lithos* **2014**, *205*, 266–283. [CrossRef]
15. Luo, Z.H.; Ke, S.; Cao, Y.Q.; Deng, J.F.; Chen, H.W. Late Indosinian mantlederived magmatism in the East Kunlun. *Geol. Bull. China* **2002**, *21*, 292–297, (In Chinese with English abstract).
16. Xiong, F.H.; Ma, C.Q.; Jiang, H.A.; Liu, B.; Zhang, J.Y.; Zhou, Q. Petrogenetic and tectonic significance of Permian calc-alkaline lamprophyres, East Kunlun orogenic belt, Northern Qinghai-Tibet Plateau. *Int. Geol. Rev.* **2013**, *55*, 1817–1834. [CrossRef]
17. Xia, R.; Wang, C.; Qing, M.; Deng, J.; Carranza, E.J.M.; Li, W.L.; Guo, X.D.; Ge, L.S.; Yu, W.Q. Molybdenite Re–Os, zircon U–Pb dating and Hf isotopic analysis of the Shuangqing Fe–Pb–Zn–Cu skarn deposit, East Kunlun Mountains, Qinghai Province, China. *Ore Geol. Rev.* **2015**, *66*, 114–131. [CrossRef]
18. He, C.F. Metallogenic geological characteristics of Kangdenongshe barite-type Au polymetallic deposit in Qinghai. *Miner. Resour. Geol.* **2014**, *28*, 399–408. (In Chinese)
19. Jiang, C.F.; Wang, Z.Q. *Opening Closing Tectonics of Central Orogenic Belt*; Geological Publishing House: Beijing, China, 2000; pp. 1–108. (In Chinese)
20. Liu, Y.; Fu, L.B.; Wang, F.L.; Wei, J.H.; Guan, B.; Tan, J.; Yang, B.R.; Wang, D.Z. Relationship Between Pb–Zn and Au–Ag Mineralization of Kengdenongshe Polymetallic Deposit in Eastern Segment of the Eastern Kunlun. *Geotecton. Metallog.* **2018**, *42*, 480–493. (In Chinese)
21. Hou, K.J.; Li, Y.H.; Zou, T.R.; Qu, X.M.; Shi, Y.R.; Xie, G.Q. Laser ablation-MC-ICPMS technique for Hf isotope microanalysis of zircon and its geological applications. *Acta Petrol. Sin.* **2007**, *23*, 2595–2604. (In Chinese)
22. Elhlou, S.; Belousova, E.; Griffin, W.L.; Pearson, N.J.; O'Reilly, S.Y. Trace element and isotopic composition of GJ red zircon standard by laser ablation. *Geochim. Cosmochim. Acta* **2006**, *70*, A158. [CrossRef]
23. Nasdala, L.; Hofmeister, W.; Norberg, N.; Martinson, J.M.; Corfu, F.; Dörr, W.; Kamo, S.L.; Kennedy, A.K.; Kronz, A.; Reiners, P.W.; et al. Zircon M257—a homogeneous natural reference material for the ion microprobe U–Pb analysis of zircon. *Geostand. Geoanal. Res.* **2008**, *32*, 247–265. [CrossRef]
24. Liu, Y.S.; Hu, Z.C.; Zong, K.Q.; Gao, C.G.; Gao, S.; Xu, J.; Chen, H.H. Reappraisement and refinement of zircon U–Pb isotope and trace element analyses by LA-ICP-MS. *Chin. Sci. Bull.* **2010**, *55*, 1535–1546. [CrossRef]
25. Liu, Y.S.; Hu, Z.C.; Gao, S.; Gunther, D.; Xu, J.; Gao, C.G.; Chen, H.H. In situ analysis of major and trace elements of anhydrous minerals by LA-ICP-MS without applying an internal standard. *Chem. Geol.* **2008**, *257*, 34–43. [CrossRef]

26. Corfu, F.; Hanchar, J.M.; Hoskin, P.; Kinny, P. Atlas of zircon textures. *Rev. Mineral. Geochem.* **2003**, *16*, 469–500. [CrossRef]
27. Yu, H.C.; Guo, C.A.; Qiu, K.F.; McIntire, D.; Jiang, G.P.; Gou, Z.Y.; Geng, J.Z.; Pang, Y.; Zhu, R.; Li, N.B. Geochronological and geochemical constraints on the formation of the giant Zaozigou Au–Sb deposit, West Qinling, China. *Minerals* **2019**, *9*, 37. [CrossRef]
28. Rollinson, H.R. *Using Geochemical Data: Evaluation, Presentation, Interpretation*; Longman Group UK Ltd.: New York, NY, USA, 1993; pp. 1–352.
29. Irvine, T.N.J.; Baragar, W.R.A. A guide to the chemical classification of the common volcanic rocks. *Can. J. Earth Sci.* **1971**, *8*, 523–548. [CrossRef]
30. Maniar, P.D.; Piccoli, P.M. Tectonic discrimination of granitoids. *Geol. Soc. Am. Bull.* **1989**, *101*, 635–643. [CrossRef]
31. Sun, S.S.; McDonough, W.F. Chemical and isotopic systematics of oceanic basalts: Implications for mantle composition and processes. *Geol. Soc. Lond. Spec. Publ.* **1989**, *42*, 313–345. [CrossRef]
32. Wang, W.; Yuan, W.M.; Gou, J.; Tian, C.S.; Ma, Z.Y.; Peng, W.X.; Feng, Y.L.; Cao, J.H.; Cheng, X.Q.; Hao, N.N. Zircon U–Pb ages and geochemical features of granites in Dulan area, Eastern Kunlun Mountains. *J. Chin. Electron Microsc. Soc.* **2015**, *34*, 222–233. (In Chinese)
33. Xia, R.; Deng, J.; Qing, M.; Li, W.L.; Guo, X.D.; Zeng, G.Z. Petrogenesis of ca. 240 Ma intermediate and felsic intrusions in the Nan'getan: Implications for crust–mantle interaction and geodynamic process of the East Kunlun Orogen. *Ore Geol. Rev.* **2017**, *90*, 1099–1117. [CrossRef]
34. Zhang, J.Y.; Ma, C.Q.; Xiong, F.H.; Liu, B. Petrogenesis and tectonic significance of the Late Permian–Middle Triassic calc-alkaline granites in the Balong region, eastern Kunlun Orogen, China. *Geol. Mag.* **2012**, *149*, 892–908. [CrossRef]
35. Jiang, Y.H.; Jia, R.Y.; Liu, Z.; Liao, S.Y.; Zhao, P.; Zhou, Q. Origin of Middle Triassic high-K calc-alkaline granitoids and their potassic microgranular enclaves from the western Kunlun orogen, northwest China: A record of the closure of Paleo-Tethys. *Lithos* **2013**, *156*, 13–30. [CrossRef]
36. Chappell, B.W.; White, A.J.R. I- and S-type granites in the Lachlan Fold Belt. *Trans. R. Soc. Edinb. Earth Sci.* **1992**, *83*, 1–26.
37. Chappell, B.W.; White, A.J.R. Two contrasting granite types: 25 years later. *Aust. J. Earth Sci.* **2001**, *48*, 489–499. [CrossRef]
38. Kemp, A.I.S.; Hawkesworth, C.J.; Foster, G.L.; Paterson, B.A.; Woodhead, J.D.; Hergt, J.M.; Gray, C.M.; Whitehouse, M.J. Magmatic and crustal differentiation history of granitic rocks from Hf\O isotopes in zircon. *Science* **2007**, *315*, 980–983. [CrossRef]
39. Stevens, G.; Villaros, A.; Moyen, J.F. Selective peritectic garnet entrainment as the origin of geochemical diversity in S-type granites. *Geology* **2007**, *35*, 9–12. [CrossRef]
40. Champion, D.C.; Bultitude, R.J. The geochemical and Sr–Nd isotopic characteristics of Paleozoic fractionated S-types granites of north Queensland: Implications for S-type granite petrogenesis. *Lithos* **2013**, *162*, 37–56. [CrossRef]
41. Clemens, J.D. S-type granite magmas—Petrogenetic issues, models and evidence. *Earth-Sci. Rev.* **2003**, *61*, 1–18. [CrossRef]
42. Chappell, B.W. Aluminium saturation in I- and S-type granites and the characterization of fractionated haplogranites. *Lithos* **1999**, *46*, 535–551. [CrossRef]
43. Bau, M. Controls on the fractionation of isovalent trace elements in magmatic and aqueous systems: Evidence from Y/Ho, Zr/Hf, and lanthanide tetrad effect. *Contrib. Mineral. Petrol.* **1996**, *123*, 323–333. [CrossRef]
44. Claiborne, L.L.; Miller, C.F.; Walker, B.A.; Wooden, J.L.; Mazdab, F.K.; Bea, F. Tracking magmatic processes through Zr/Hf ratios in rocks and Hf and Ti zoning inzircons: An example from the Spirit Mountain batholith, Nevada. *Mineral. Mag.* **2006**, *70*, 517–543. [CrossRef]
45. Ballouard, C.; Poujol, M.; Boulvais, P.; Branquet, Y.; Tartèse, R.; Vigneresse, J.L. Nb–Ta fractionation in peraluminous granites: A marker of the magmatic-hydrothermal transition. *Geology* **2016**, *44*, 231–234. [CrossRef]
46. Wu, F.Y.; Jahn, B.M.; Wilde, S.A.; Lo, C.H.; Yui, T.F.; Lin, Q.; Ge, W.C.; Sun, D.Y. Highly fractionated I-type granites in NE China (I): Geochronology and petrogenesis. *Lithos* **2003**, *66*, 241–273. [CrossRef]
47. Qiu, K.F.; Deng, J. Petrogenesis of granitoids in the Dewulu skarn copper deposit: Implications for the evolution of the Paleotethys ocean and mineralization in Western Qinling, China. *Ore Geol. Rev.* **2017**, *90*, 1078–1098. [CrossRef]

48. Liu, Y.; Chakhmouradian, A.R.; Hou, Z.Q.; Song, W.L.; Kynický, J. Development of REE mineralization in the giant Maoniuping deposit (Sichuan, China): Insights from mineralogy, fluid inclusions, and trace-element geochemistry. *Miner. Depos.* **2019**, *54*, 701–718. [CrossRef]
49. Zeng, Y.C.; Xu, J.F.; Ducea, M.N.; Chen, J.L.; Huang, F.; Zhang, L. Initial rifting of the Lhasa Terrane from Gondwana: Insights from the Permian (~262 Ma) amphibole-rich lithospheric mantle-derived Yawa basanitic intrusions in southern Tibet. *J. Geophys. Res. Solid Earth* **2019**, *124*, 2564–2581. [CrossRef]
50. Inger, S.; Harris, N. Geochemical constraints on Leucogranite magmatism in the Langtang Valley, Nepal Himalaya. *J. Petrol.* **1993**, *34*, 345–368. [CrossRef]
51. Patiño Douce, A.E.; Harris, N. Experimental constraints on Himalayan anatexis. *J. Petrol.* **1998**, *39*, 689–710. [CrossRef]
52. Gao, L.E.; Zeng, L.S.; Asimow, P.D. Contrasting geochemical signatures of fluid-absent versus fluid-fluxed melting of muscovite in metasedimentary sources: The Himalayan leucogranites. *Geology* **2017**, *45*, 39–42. [CrossRef]
53. Xin, Y.J.; Li, J.H.; Dong, S.W.; Zhang, Y.Q.; Wang, W.B.; Sun, H.S. Neoproterozoic post-collisional extension of the central Jiangnan Orogen: geochemical, geochronological, and Lu–Hf isotopic constraints from the ca. 820–800 Ma magmatic rocks. *Precambr. Res.* **2017**, *294*, 91–110. [CrossRef]
54. Rapp, R.P.; Watson, E.B. Dehydration melting of metabasalt at 8–32 kbar: Implications for continental growth and crust–mantle recycling. *J. Petrol.* **1995**, *36*, 891–931. [CrossRef]
55. Sylvester, P.J. Post-collisional strongly peraluminous granites. *Lithos* **1998**, *45*, 29–44. [CrossRef]
56. Zhu, R.Z.; Lai, S.C.; Qin, J.F.; Zhao, S.W.; Santosh, M. Strongly peraluminous fractionated S-type granites in the Baoshan Block, SW China: Implications for two-stage melting of fertile continental materials following the closure of Bangong-Nujiang Tethys. *Lithos* **2018**, *316*, 178–198. [CrossRef]
57. Huang, L.C.; Jiang, S.Y. Highly fractionated S-type granites from the giant Dahutang Tungsten deposit in Jiangnan orogen, southeast China: Geochronology, petrogenesis and their relationship with W-mineralization. *Lithos* **2014**, *202–203*, 207–226. [CrossRef]
58. Qiu, K.F.; Taylor, R.D.; Song, Y.H.; Yu, H.C.; Song, K.R.; Li, N. Geologic and geochemical insights into theformation of the Taiyangshan porphyry copper-molybdenum deposit, Western Qinling Orogenic Belt, China. *Gondwana Res.* **2016**, *35*, 40–58. [CrossRef]
59. Zeng, Y.C.; Xu, J.F.; Chen, J.L.; Wang, B.D.; Kang, Z.Q.; Huang, F. Geochronological and geochemical constraints on the origin of the Yunzhug ophiolite in the Shiquanhe–Yunzhug–Namu Tso ophiolite belt, Lhasa Terrane, Tibetan Plateau. *Lithos* **2018**, *300*, 250–260. [CrossRef]
60. Wang, X.S.; Gao, J.; Klemd, R.; Jiang, T.; Zhai, Q.G.; Li, J.L.; Liang, X.Q. From arc accretion to continental collision in the eastern Jiangnan Orogen: Evidence from two phases of S-type granites. *Precambrian Res.* **2019**, *321*, 199–211. [CrossRef]
61. Wang, Y.J.; Xing, X.X.; Cawood, P.A.; Lai, S.C.; Xia, X.P.; Fan, W.M.; Liu, H.C.; Zhang, F.F. Petrogenesis of early Paleozoic peraluminous granite in the Sibumasu Block of SW Yunnan and diachronous accretionary orogenesis along the northern margin of Gondwana. *Lithos* **2013**, *182–183*, 67–85. [CrossRef]
62. Altherr, R.; Holl, A.; Hegner, E.; Langer, C.; Kreuzer, H. High-potassium, calc-alkaline I-type plutonism in the European Variscides: Northern Vosges (France) and northern Schwarzwald (Germany). *Lithos* **2000**, *50*, 51–73. [CrossRef]
63. Pan, Y.S.; Zhou, W.M.; Xu, R.H.; Wang, D.A.; Zhang, Y.Q.; Xie, Y.W.; Chen, T.E.; Luo, H. Geological characteristics and evolution of Kunlun Mountains in the Early Paleozoic. *Sci. China (Ser. D)* **1996**, *26*, 302–307. (In Chinese)
64. Wang, G.C.; Wang, Q.H.; Jian, P.; Zhu, Y.H. Zircon SHRIMP ages of Precambrian metamorphic basement rocks and their tectonic significance in the eastern Kunlun Mountains, Qinghai Province, China. *Earth Sci. Front.* **2004**, *11*, 481–490. (In Chinese)
65. Li, R.B.; Pei, X.Z.; Li, Z.C.; Sun, Y.; Pei, L.; Chen, G.C.; Chen, Y.X.; Liu, C.J.; Wei, F.H. Regional tectonic transformation in East Kunlun orogenic belt in Early Paleozoic: Constraints from the geochronology and geochemistry of Helegangnaren alkali-feldspar granite. *Acta Geol. Sin.* **2013**, *87*, 333–345.
66. Li, R.B.; Pei, X.Z.; Pei, L.; Li, Z.C.; Chen, G.C.; Chen, Y.X.; Liu, C.; Wang, M. The Early Triassic Andean-type Halagatu granitoids pluton in the East Kunlun orogen, northern Tibet Plateau: Response to the northward subduction of the Paleo-Tethys Ocean. *Gondwana Res.* **2018**, *62*, 212–226. [CrossRef]

67. Yang, J.S.; Wang, X.B.; Shi, R.D.; Xu, Z.Q.; Wu, C.L. The Dur'ngoi ophiolite in East Kunlun, northern Qinghai-Tibet Plateau: A fragment of Paleo-Tethyan oceanic crust. *Geol. China* **2004**, *31*, 225–239. (In Chinese)
68. Lu, L.; Wu, Z.H.; Hu, D.G.; Barosh, P.J.; Hao, S.; Zhou, C.J. Zircon U–Pb age forrhyolite of the Maoniushan formation and its tectonic significance in the EastKunlun Mountains. *Acta Petrol. Sin.* **2010**, *26*, 1150–1158.
69. Liu, Z.Q.; Pei, X.Z.; Li, R.B.; Li, Z.C.; Zhang, X.F. LA-ICP-MS Zircon U–Pb geochronology of the two suites of ophiolites at the Buqingshn area of the A'nyemaqen orogenic belt in the southern margin of East Kunlun and its tectonic implication. *Acta Geol. Sin.* **2011**, *85*, 185–194. (In Chinese)
70. Li, S.Z.; Zhao, S.J.; Li, X.Y.; Cao, H.H.; Guo, X.Y.; Xiao, W.J.; Lai, S.C.; Yan, Z.; Li, Z.H.; Yu, S.Y.; et al. Proto-Tethys Ocean in East Asia (I): Northern and southern border faults and subduction polarity. *Acta Petrol. Sin.* **2016**, *32*, 2609–2627. (In Chinese)
71. Li, S.; Zhao, S.; Liu, X.; Cao, H.; Yu, S.; Li, X.; Somerville, I.; Yu, S.; Suo, Y. Closure of the Proto-Tethys Ocean and Early Paleozoic amalgamation of microcontinental blocks in East Asia. *Earth-Sci. Rev.* **2018**, *186*, 37–75. [CrossRef]
72. Xiong, F.H.; Ma, C.Q.; Zhang, J.Y.; Liu, B.; Jiang, H.A.; Huang, J. Zircon LA-ICP-MS U–Pb dating of Bairiqili gabbro pluton in East Kunlun orogenic belt and its geological significance. *Geol. Bull. China* **2011**, *30*, 1196–1202. (In Chinese)
73. Xiong, F.H.; Ma, C.Q.; Zhang, J.Y.; Liu, B. The origin of mafic microgranular enclaves and their host granodiorites from East Kunlun, Northern Qinghai-Tibet Plateau: Implications for magma mixing during subduction of Paleo-Tethyan lithosphere. *Mineral. Petrol.* **2012**, *104*, 211–224. [CrossRef]
74. Chen, H.W.; Luo, Z.H.; MO, X.X.; Liu, C.D.; Ke, S. Underplating mechanism of Triassic granite of magm mixing origin in the East Kunlun orogenic belt. *Chin. Geol.* **2005**, *32*, 390–395. (In Chinese with English abstract)
75. Roger, F.; Arnaud, N.; Gilder, S.; Tapponnier, P.; Jolivet, M.; Brunel, M.; Malavieille, J.; Xu, Z.; Yang, J. Geochronological and geochemical constraints on Mesozoic suturing in east central Tibet. *Tectonics* **2003**, *22*, 1037. [CrossRef]
76. Mo, X.X.; Luo, Z.H.; Deng, J.F.; Yu, X.H.; Liu, C.D.; Chen, H.W.; Yuan, W.M.; Liu, Y.H. Granitoids and crustal growth in the East-Kunlun orogenic belt. *Geol. J. China Univ.* **2007**, *13*, 403–414. (In Chinese)
77. Gehrels, G.; Kapp, P.; DeCelles, P.; Pullen, A.; Blakey, R.; Weislogel, A.; Ding, L.; Guynn, J.; Martin, A.; McQuarrie, N.; et al. Detrital zircon geochronology of pre-Tertiary strata in the Tibetan-Himalayan orogen. *Tectonics* **2011**, *30*, C5016. [CrossRef]
78. Ding, Q.F.; Liu, F.; Yan, W.; Li, B.L.; Sun, F.Y. Zircon U–Pb geochronology and Hf isotopic constraints on the petrogenesis of Early Triassic granites in the Wulonggou area of the Eastern Kunlun Orogen, Northwest China. *Int. Geol. Rev.* **2015**, *57*, 1735–1754. [CrossRef]
79. Li, X.; Huang, X.; Luo, M.; Dong, G.; Mo, X. Petrogenesis and geodynamic implications of the Mid-Triassic lavas from East Kunlun, northern Tibetan Plateau. *J. Asian Earth Sci.* **2015**, *105*, 32–47. [CrossRef]
80. Qiu, K.F.; Yu, H.C.; Wu, M.Q.; Geng, J.Z.; Ge, X.K.; Gou, Z.Y.; Ryan, D.T. Discrete Zr and REE mineralization of the Baerzhe rare-metal deposit, China. *Am. Mineral.* **2019**. [CrossRef]
81. Gou, Z.Y.; Yu, H.C.; Qiu, K.F.; Geng, J.Z.; Wu, M.Q.; Wang, Y.G.; Yu, M.H.; Li, J. Petrogenesis of ore-hosting diorite in the Zaorendao gold deposit at the Tongren-Xiahe-Hezuo polymetallic district, West Qinling, China. *Minerals* **2019**, *9*, 76. [CrossRef]
82. Ju, Y.J.; Zhang, X.L.; Lai, S.C.; Qin, J.F. Permian–Triassic highly-fractionated I-type granites from the southwestern Qaidam Basin (NW China): Implications for the evolution of the paleo-tethys in the eastern Kunlun orogenic belt. *J. Earth Sci.* **2017**, *28*, 51–62. [CrossRef]
83. Winter, J.D. *Pricinples of Igneous and Metamorphic Petrology*, 2nd ed.; PHI: Washington, DC, USA, 2013; pp. 1–702.
84. Barbarin, B. A review of the relationships between granitoid types, their origins and their geodynamic environments. *Lithos* **1999**, *46*, 605–626. [CrossRef]
85. Yan, Z.; Bian, Q.T.; Korchagin, O.A.; Pospelov, I.I.; Li, J.L.; Wang, Z.Q. Provenance of Early Triassic Hongshuichuan Formation in the southern margin of the East Kunlun Mountains: Constrains from detrital framework, heavy mineral analysis and geochemistry. *Acta Petrol. Sin.* **2008**, *24*, 1068–1079.
86. Li, R.B.; Pei, X.Z.; Li, Z.C.; Liu, Z.Q.; Chen, G.C.; Chen, Y.X.; Wei, F.H.; Gao, J.M.; Liu, C.J. Geological characteristics of Late Palaeozoic-Mesozoic unconformities and their response to some significant tectonic events in eastern part of Eastern Kunlun. *Earth Sci. Front.* **2012**, *19*, 244–254. (In Chinese)

87. Liu, Y.J.; Genser, J.; Neubauer, F.; Jin, W.; Ge, X.H.; Handler, R.; Takasu, A. $^{40}Ar/^{39}Ar$ mineral ages from basement rocks in the eastern Kunlun Mountains, NW China, and their tectonic implications. *Tectonophysics* **2005**, *398*, 199–224. [CrossRef]
88. Jiang, G.M. Study on the Genesis and Metallogenic Regularity of Kengdenongshe Au–Pb–Zn Polymetallic Deposit, Maduo County, Qinghai Province. Ph.D. Thesis, Central South University, Changsha, China, 2014. (In Chinese)
89. Chen, G.C. Petrology, Genesis and Geological Significance of Late Paleozoic-Early Mesozoic Granitoids in East Kunlun Orogen. Ph.D. Thesis, Chang'an University, Xi'an, China, 2014. (In Chinese)
90. Gao, Y.B. The Intermediate-acid Intrusive Magmatism and Mineralization in Qimantag, East Kunlun Moutains. Ph.D. Thesis, Chang'an University, Xi'an, China, 2013. (In Chinese)